Photon-Number-Resolution at Telecom Wavelength with Superconducting Nanowires

Francesco Marsili[1,2], David Bitauld[2], Andrea Fiore[2],
Alessandro Gaggero[3], Francesco Mattioli[3], Roberto Leoni[3],
Aleksander Divochiy[4] and Gregory Gol'tsman[4]
[1]Ecole Polytechnique Fédérale de Lausanne (EPFL), Institute of Photonics and Quantum Electronics (IPEQ), Station 3, CH-1015 Lausanne,
[2]COBRA Research Institute, Eindhoven University of Technology, P.O. Box 513, NL-5600MB Eindhoven,
[3]Istituto di Fotonica e Nanotecnologie (IFN), CNR, via Cineto Romano 42, 00156 Roma,
[4]Moscow State Pedagogical University (MSPU), Department of Physics, 119992 Moscow,
[1]Switzerland
[2]The Netherlands
[3]Italy
[4]Russian Federation

1. Introduction

Optical detection involves converting an optical signal into an electrical signal. Most optical detectors are operated in a linear mode, i.e. the output signal is proportional to the incident photon flux. The main limitation in sensitivity of these linear detectors is the ability to extract a small signal from the amplifier noise in a given bandwidth. For example, avalanche photodiodes (APDs) commonly used in fiber-based optical communications have sensitivities of few hundreds of photons in a 100 ps detection window. When higher sensitivities are needed, single-photon detectors (SPDs) are often used, which operate in a strongly nonlinear mode. Indeed, a pulse containing more than one photon produces the same output signal as a single-photon pulse, which implies that it is not possible to directly measure the number n of photons in a pulse, if the pulse duration is smaller than the detector response time. However, photon number resolving (PNR) detectors are important in quantum communication, quantum information processing and quantum optics for two class of applications. In one case PNR detectors are needed to reconstruct the incoming photon number statistics by ensemble measurements. This is the case of the characterization of nonclassical light sources such as single photon (Yuan et al. 2002) or n-photon (Waks et al. 2004) state generators or of the detection of pulse splitting attacks in quantum cryptography (Brassard et al. 2000). In the second case PNR detectors are needed to perform a single-shot measurement of the photon number. Applications of this kind are linear-optics quantum computing (Knill et al. 2001), long distance quantum communication (which requires quantum repeaters (Sangouard et al. 2007)) and conditional-state preparation (Sliwa &

Banaszek 2003). Moreover, a linear detector with single-photon sensitivity can also be used for measuring a temporal waveform at extremely low light levels, e.g. in long-distance optical communications, fluorescence spectroscopy, and optical time-domain reflectometry. Among the approaches proposed so far to PNR detection, detectors based on charge-integration or field-effect transistors (Fujiwara & Sasaki 2007; Gansen et al. 2007; Kardynal et al. 2007) are affected by long integration times, leading to bandwidths <1 MHz. Transition edge sensors (TES (Lita et al. 2008)) show extremely high (95%) detection efficiencies but they operate at 100 mK and show long response times (several hundreds of nanoseconds in the best case). Approaches based on photomultipliers (PMTs) (Zambra et al. 2004) and APDs, such as the visible light photon counter (VLPC) (Waks et al. 2003; Waks et al. 2004), 2D arrays of APDs (Yamamoto et al. 2006; Jiang et al. 2007) and time-multiplexed detectors (Achilles et al. 2003; Fitch et al. 2003) are not sensitive or are plagued by high dark count rate and long dead times in the telecommunication spectral windows. Arrays of single photon detectors SPDs additionally involve complex read-out schemes (Jiang et al. 2007) or separate contacts, amplification and discrimination (Dauler et al. 2007). We recently demonstrated an alternative approach (Divochiy et al. 2008; Marsili et al. 2009a), the Parallel Nanowire Detector (PND), which uses spatial multiplexing on a subwavelength scale to provide a single electrical output proportional to the photon number. The device presented significantly outperforms existing PNR detectors in terms of simplicity, sensitivity, speed, and multiplication noise (Divochiy et al. 2008). Here we present the working principle of the device (section 2), its fabrication process (section 3), the results of the optical characterization (section 4), an analysis of the device operation and corresponding design guidelines (section 5) and the first application of a PND to reconstruct an unknown incoming photon number statistics (section 6).

2. Photon number resolution principle

The structure of PNDs is the parallel connection of N superconducting nanowires (N-PND), each of which can be connected in series to a resistor R_0 (N-PND-R, Figure 1a). The detecting element is a 4-6 nm thick, 100 nm wide NbN wire folded in a meander pattern. Each section acts as a nanowire superconducting single photon detector (SSPD) (Verevkin et al. 2002). In SSPDs, if a superconducting nanowire is biased close to its critical current, the absorption of a photon causes the formation of a normal barrier across its cross section, so almost all the bias current is pushed to the external circuit. In PNDs, the currents from different sections can sum up on the external load, producing an output voltage pulse proportional to the number of photons absorbed.

The time evolution of the device after photon absorption can be simulated using the equivalent circuit of Figure 1b. Each section is modeled as the series connection of a switch which opens on the hotspot resistance R_{hs} for a time t_{hs}, simulating the absorption of a photon, of an inductance L_{kin}, accounting for kinetic inductance (Kadin) and of a resistor R_0. The device is connected through a bias T to the bias current source I and to the input resistance of the preamplifier R_{out}. The n firing sections, in red, all carry the same current I_f and the N-n still superconducting sections (unfiring), in blue, all carry the same current I_u. I_{out} is the current flowing through R_{out}. Let I_B be the bias current flowing through each section when the device is in the steady state. If a photon reaches the ith nanowire, it will cause the superconducting-normal transition with a probability $\eta_i = \eta(I_B/I_C^{(i)})$, where η is the current-dependent detection efficiency and $I_C^{(i)}$ is the critical current of the nanowire

(Verevkin et al. 2002) (the nanowires have different critical currents, being differently constricted (Kerman et al. 2007)). Because of the sudden increase in the resistance of firing nanowire, its current (I_f) is redistributed between the other N-1 unfiring branches and R_{out}. This argument yields that if n sections fire simultaneously (in a time interval much shorter than the current relaxation time), part of their currents sum up on the external load.
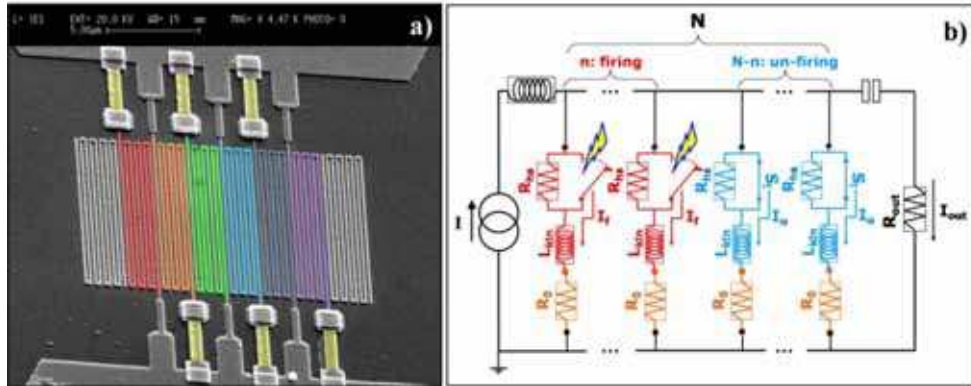

Fig. 1. (a) Scanning electron microscope (SEM) image of a PND with N=6 and series resistors (6-PND-R) fabricated on a 4nm thick NbN film on MgO. The nanowire width is w=100 nm, the meander fill factor is f=40%. The detector active area is Ad=10x10 µm². The devices are contacted through 70nm thick Au-Ti pads, patterned as a 50 Ω coplanar transmission line. The active nanowires (in color) of the PND-R are connected in series with Au-Pd resistors (in yellow). The floating meanders at the two edges of the PND-R pixel are included to correct for the proximity effect. (b) Circuit equivalent of a N-PND-R. The n firing sections, in red, all carry the same current I_f and the N-n still superconducting sections (unfiring), in blue, all carry the same current I_u. I_{out} is the current flowing through the input resistance R_{out} of the preamplifier. From (Marsili et al. 2009b).

The device shows PNR capability if the height of the current pulse through R_{out} for n firing stripes $\bar{I}_{out}^{(n)}$ is n times higher than the pulse for one $\bar{I}_{out}^{(1)}$, i.e. if the leakage current drained by each of the unfiring nanowires $\delta I_{lk}=I_u-I_B$ is negligible with respect to I_B. The leakage current is also undesirable because it lowers the signal available for amplification and temporary increases the current flowing through the still superconducting (unfiring) sections, eventually driving them normal. Consequently, δI_{lk} limits the maximum bias current allowed for the stable operation of the device and then the detection efficiencies of the sections. The leakage current depends on the ratio between the impedance of a section Z_S and R_{out} and it can be reduced by engineering the dimensions of the nanowire (thus its kinetic inductance) and of the series resistor (see sec. 5). The design without series resistors simplifies the fabrication process, but, as Z_S is lower, δI_{lk} significantly limits the detection efficiency of the device.

3. Fabrication

NbN films 3-4 nm thick were grown on sapphire (substrate temperature T_S=900°C (Gol'tsman et al. 2003; Gol'tsman et al. 2007)) or MgO (T_S=400°C (Marsili et al. 2008))

substrates by reactive magnetron sputtering in an argon–nitrogen gas mixture. Using an optimized sputtering technique, our NbN samples exhibited a superconducting transition temperature of T_C =10.5 K for 40-Å-thick films. The superconducting transition width was ΔT_C = 0.3 K.

Both the designs with and without the integrated bias resistors were implemented. Detector size ranges from 5x5 µm^2 to 10x10 µm^2 with the number of parallel branches varying from 4 to 14. The nanowires are 100 to 120 nm wide and the fill factor of the meander is 40 to 60%. The length of each nanowire ranges from 25 to 100 µm.

For the devices on MgO, the three nanolithography steps needed to fabricate the structure have been carried out by using an electron beam lithography (EBL) system equipped with a field emission gun (acceleration voltage 100 kV, 20 nm resolution). In the first step e-beam lithography is used to define pads (patterned as a 50 Ω coplanar transmission line) and alignment markers on a 450nm-thick polymethyl methacrylate (PMMA, a positive tone electronic resist) layer. The sample is then coated with a Ti-Au film (60 nm Au on 10nm Ti) deposited by e-gun evaporation, which is selectively removed by lift-off from un-patterned areas. In the second step, a 160nm thick hydrogen silsesquioxane (HSQ FOX-14, a negative tone electronic resist) mask is defined reproducing the meander pattern. The alignment between the different layers is performed using the markers deposited in the first lithography step. All the unwanted material, i.e. the material not covered by the HSQ mask and the Ti/Au film, is removed by using a fluorine based (CHF_3+SF_6+Ar) reactive ion etching (RIE). Finally, with the third step the series resistors (85nm AuPd alloy, 50%-each in weight), aligned with the two previous layers, are fabricated by lift off via a PMMA stencil mask. Our process is optimized to obtain both an excellent alignment between the different e-beam nanolithography steps (error of the order of 100 nm) and a nanowire with high width uniformity (less than 10% (Mattioli et al. 2007)).

Details on the fabrication process of the devices on sapphire can be found in (Gol'tsman et al. 2007).

4. Device optical characterization

In this section we present the results of the optical characterization of PNDs and PND-Rs (Divochiy et al. 2008), i.e. their speed performance (section 4.2), the proof of their PNR capability and their detection efficiency at λ=1.3 µm (section 4.3).

4.1 Measurement setup

Electrical and optical characterizations have been performed in a cryogenic probe station with an optical window and in cryogenic dipsticks. The bias current was supplied through the DC port of a 10MHz-4GHz bandwidth bias-T connected to a low noise voltage source in series with a bias resistor. The AC port of the bias-T was connected to the room-temperature, low-noise amplifiers. The amplified signal was fed either to a 1 GHz bandwidth single shot oscilloscope, a 40 GHz bandwidth sampling oscilloscope, or a 150MHz bandwidth counter for time resolved measurements and statistical analysis. The devices were optically tested using a fiber-pigtailed, gain-switched laser diode at 1.3 µm wavelength (100ps-long pulses, repetition rate 26 MHz), a mode-lock Ti:sapphire laser at 700 nm wavelength (40ps-long pulses, repetition rate 80 MHz), or an 850 nm GaAs pulsed laser (30 ps-long pulses, repetition rate 100 kHz).

In the cryogenic probe station (Janis) the devices were tested at a temperature T=5 K. Electrical contact was realized by a cooled 50 Ω microwave probe attached to a micromanipulator, and connected by a coaxial line to the room-temperature circuitry. The light was fed to the PNDs through a single-mode optical fiber coupled with a long working distance objective, allowing the illumination of a single detector.

In the cryogenic dipsticks the devices were tested at 4.2 K or 2 K. The light was sent through a single-mode optical fiber either put in direct contact and carefully aligned with the active area of a single device or coupled with a short focal length lens, placed far from the plane of the chip to ensure uniform illumination. The number of incident photons per device area was estimated with an error of 5 %.

Throughout the paper, the single photon detection efficiency of an N-PND ($\tilde{\eta}$) or of one of its sections (η) are defined with respect to the photon flux incident on the area covered by the device (active area A_d, typically 10 x 10 μm^2) or by one section (A_d/N), respectively.

4.2 Speed performance

Figure 2.a shows a single-shot oscilloscope trace of the photoresponse of a 8.6x8 μm^2 5-PND under laser illumination (λ=700 nm, 80 MHz repetition rate). Pulses with five different amplitudes can be observed, corresponding to the transition of one to five sections. The measured 80 MHz counting rate represents an improvement of three orders of magnitude over most of the PNR detectors at telecom wavelength (Rosenberg et al. 2005; Fujiwara & Sasaki 2007; Jiang et al. 2007), with the only exception of the SSPD array (Dauler et al. 2007).
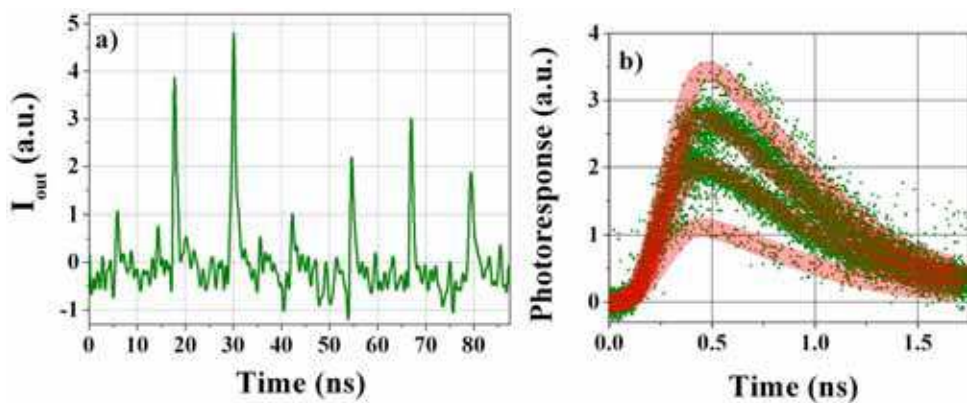

Fig. 2. a. Single-shot oscilloscope trace during photodetection by a 8.6x8 µm2 5-PND. The device was tested under uniform illumination in a cryogenic dipstick dipped in a liquid He bath at 4.2 K. The light pulses at 700 nm form a mode-locked Ti:sapphire laser had a repetition rate of 80 MHz. b. Photoresponse transients taken with a 40 GHz sampling oscilloscope while probing a 10x10 µm2 4-PND-R in the cryogenic probe station under illumination with 1.3 µm, 100ps-long pulses from a laser diode, at a repetition rate of 26MHz. The solid curves are guides to the eyes. From (Marsili et al. 2009b).

We investigated the temporal response of a 10x10 μm² 4-PND-R probed with light at 1.3 μm wavelength using a 40 GHz sampling oscilloscope (Figure 2.b). All four possible amplitudes can be observed. The pulses show a full width at half maximum (FWHM) as low as 660ps. In a traditional 10x10 μm² SSPD, the pulse width would be of the order of 10 ns FWHM, so the recovery of the output current I_{out} through the amplifier input resistance is a factor ~4² faster (see section 5.3), which agrees with results reported by other groups (Gol'tsman et al. 2007; Tarkhov et al. 2008). As shown in section 5.3, the very attractive N² scaling rule for the output pulse duration unfortunately does not apply to the device recovery time.

4.3 Proof of PNR capability

Let an *N*-PND be probed with a light whose photon number probability distribution is **S**=[S(*m*)]=[s$_m$]. The probability distribution of the number of measured photons **Q**=[Q(*n*)]=[q$_n$] is related to **S** by the relation:

$$Q(n) = \sum_m P^N(n \mid m) \cdot S(m) \qquad (1)$$

where $P^N(n|m)$ is the probability that *n* photons are detected when *m* are sent to the device.

To infer whether a PND is able to measure the number of incoming photons, it can be probed with a Poissonian distribution S(*m*)=μ^m·exp(-μ)/*m*! (μ: mean photon number). The limited efficiency η<1 of the detector is equivalent to an optical loss, and reduces the mean photon number to: μ*=ημ. In the regime μ*<<1, $S(m) \sim \left(\mu^*\right)^m / m!$, and for μ* low enough (1) can be written as:

$$Q(n) \sim P(n \mid n) \cdot S(n) \propto \left(\mu^*\right)^n / n! \qquad \qquad for\, \mu^* << 1 \qquad (2)$$

Consequently, the probability Q(1) of detecting one photon is proportional to μ, Q(2) is proportional to μ², and so on.

A 10x10 μm² 5-PND-R was tested with the coherent light of GaAs pulsed laser (λ=850 nm, 30 ps pulse width, 100kHz repetition rate), whose photon number distribution is close to a Poissonian. The photoresponse from the device was sent to a 150 MHz counter. The detection probabilities relative to one-, two- and three-photon absorption events are plotted for μ varying from 0.15 to 40 in Figure 3.a. As the mean single-photon detection efficiency $\tilde{\eta}$ of the device (defined with respect to the photon flux incident on the total active area covered by the device A$_d$) is a few percent (Figure 3.b) and μ is a few tens, the condition ημ=μ*<<1 is verified and (2) is therefore valid. Indeed, the fittings clearly show that $Q(1) \propto \mu$, $Q(\mu,2) \propto \mu^2$ and $Q(\mu,3) \propto \mu^3$, which demonstrates the capability of the detector to resolve one, two and three photons simultaneously absorbed.

The device mean single-photon detection efficiency $\tilde{\eta}$ at λ=1.3 μm and the dark-counts rate DK were measured as a function of the bias current at T= 2.2 K (Figure 3.b). The lowest DK value measured was 0.15 Hz for $\tilde{\eta}$=2% (yielding a noise equivalent power (Miller et al. 2003) NEP=4.2x10^{-18} W/Hz$^{1/2}$), limited only by the room temperature background radiation coupling to the PND. This sensitivity outperforms most of the other approaches by one-two orders of magnitude (with the only exception of transition-edge sensors (Rosenberg et al. 2005), which require a much lower operating temperature).
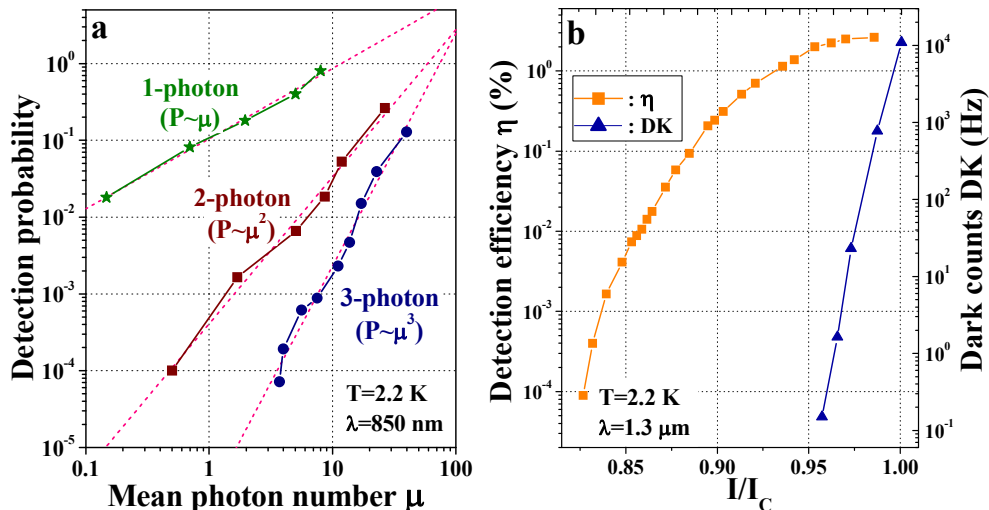
Fig. 3. a. Detection probabilities of a 10x10 μm² 5-PND-R relative to the one (stars), two (squares) and three-photon (circles) absorption events as a function of the mean photon number per pulse μ. device was mounted in cryogenic dipstick dipped in a liquid He bath at 2.2 K. A single-mode optical fiber was put in direct contact and aligned with the active area of the device. The power level was set with a variable fiber-based optical attenuator. b. Mean detection efficiency at 1.3 μm and dark-counts rate vs bias current of a 10x10 μm² 5-PND-R. The device was fiber-coupled and mounted on a cryogenic dipstick dipped in a liquid He bath at 2.2 K.

5. PND design

In this section, we provide a detailed analysis of the device operation and guidelines for the design of PNDs with optimized performance in terms of efficiency, speed and sensitivity (see also (Marsili et al. 2009b)).

The first step is to define the relevant parameter space. The width of the nanowire (w=100 nm) and the filling factor (f=50%) of the meander are fixed by technology, the thickness of the superconducting film (t=4nm) is the optimum value yielding the maximum device efficiency and the active area (A_d=10 x 10 μm²) is fixed by the size of the core of single mode fibers to which the device must be coupled. We consider single-pass geometries (no optical cavity), but the same guidelines can be applied to cavity devices with optimized absorption (Rosfjord et al. 2006). The parameters of the PND-R that can be used as free design variables are: the number of sections in parallel N, the value of the series resistor R_0 and the value of the inductance of each section L_0. The number of sections in parallel N can be chosen within a discrete set of values (N=2, 3, 4, 6, 7, 10, 17), which satisfy the constraints of w, f, size of the pixel and that the number of stripes in each sections is to be odd (we consider the geometry of Figure 1a). The value of L_0 is the sum of the kinetic inductance of each meander L_{kin} and of a series inductance which can be eventually added. L_{kin} is not a design parameter, as it is fixed by w, t, f, A_d and N. If no series inductors are added (bare devices, L_0=L_{kin}), the value of L_0 for each N is listed in Table 1.

N	L_0	SQ
2	225 nH	2500
3	153 nH	1700
4	117 nH	1300
6	81 nH	900
7	63 nH	700
10	45 nH	500
17	27 nH	300

Table 1. Inductance (L_0) and number of squares (SQ) of each section for all possible values of N. The width of the nanowires is w=100 nm, the thickness is t=4 nm. The kinetic inductance per square was estimated ($L_{kin}/\square$=90 pH) from the time constant of the exponential decay of the output current ($\tau_{out}=\tau_f=L_{kin}/R_{out}$, see sec. 5.3) for a standard 5x5µm² SSPD (Marsili et al. 2008).

An additional free parameter, relative to the read-out, is the impedance seen by the device on the RF section of the circuit R_{out}, which is 50 Ω (of the matched transmission line) in the actual measurement setup (see section 4.1), but which can be varied from zero to infinite introducing a cold preamplifier stage.

The target performance specifications are the single-photon detection efficiency (η), the signal to noise ratio (SNR) and the maximum repetition rate (speed), which must be optimized under the constraints that the operation of the device is stable and that it is possible to detect a certain maximum number of photons (n_{max}) dependent on the specific application.

This section is organized as follows. First we present the electrical equivalent model of the device developed to study its working principle and to define design guidelines (section 5.1). Then we define the figures of merit of the device performance in terms of efficiency (section 5.2), speed (section 5.3) and sensitivity (section 5.4) and we analyze their dependency on the design parameters (L_0, R_0, R_{out}, N).

5.1 Electrical model

Although a comprehensive description of PND operation should combine thermal and electrical modeling of the nanowires (Yang et al. 2007), it is possible to use a purely electrical model (see section 2 and Figure 1b) to make a reliable guess on how the device performance varies when moving in the parameter space (Marsili et al. 2009b).

In this model, the dependence of L_{kin} on the current flowing through the nanowire was disregarded, and it was assumed constant. Furthermore, it has been shown (Yang et al. 2007) that changing the values of the kinetic inductance of an SSPD or of a resistor connected in series to it results in a change of the hotspot resistance and of its lifetime, eventually causing the device to latch to the normal state. The simplified analysis presented here does not take into account these effects, and considers both R_{hs} and t_{hs} as constant (R_{hs}=5.5 kΩ, t_{hs}=250ps), and that device cannot latch. However, the results of this approach can still quantitatively predict the behavior of the device in the limit where the fastest time constant of the circuit τ_f (see section 5.3) is much higher than the hotspot lifetime ($\tau_f \gg t_{hs}$), and give a reasonable qualitative understanding of the main trends of variation of the performance of faster devices ($\tau_f \sim t_{hs}$).
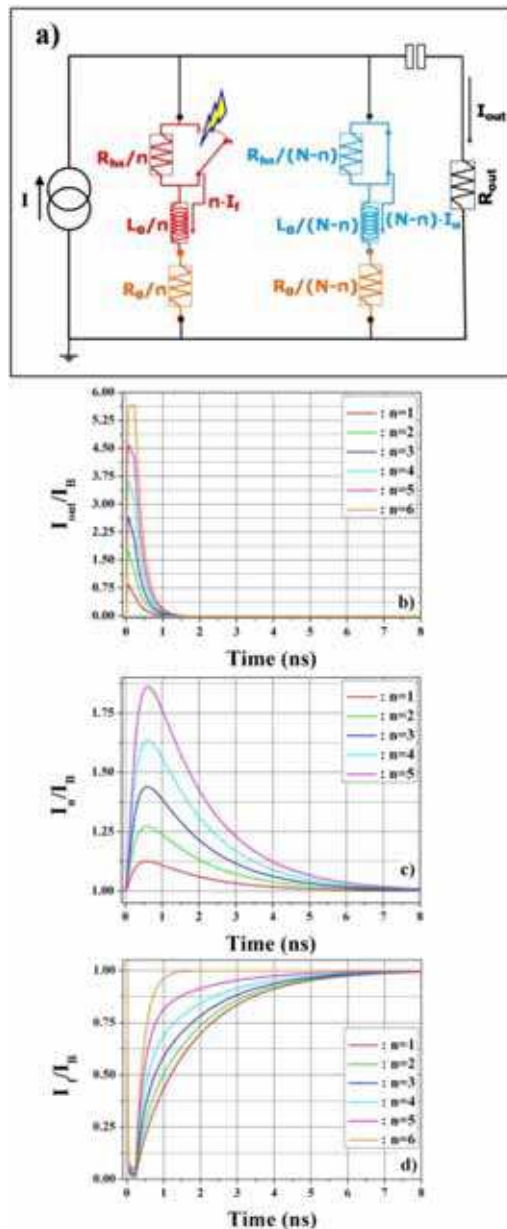
Fig. 4. (a) Simplified circuit of a N-PND-R, where the two sets of n firing and the N-n unfiring sections have been substituted by their Thévenin-equivalents. (b-d) Simulated time evolution of I_u (b), I_{out} (c) and I_f (d) for a 6-PND-R as n increases from 1 to 6. The parameters of the circuit are: $L_0=L_{kin}=81$ nH, $R_0=50$ Ω, $R_{out}=50$ Ω, $R_{hs}=5.5$ kΩ, and $t_{hs}=250$ps. From (Marsili et al. 2009b).

To gain a better insight on the circuit dynamics (see sec. 5.3) and to reduce the calculation time, the $N+1$ mesh circuit of Figure 1.b can be simplified to the three mesh circuit of Figure 4.a applying the Thévenin theorem on the n firing sections and on the remaining N-n still superconducting (unfiring) sections, separately. Figure 4.b to d show the simulation results for the time evolution of the currents flowing through R_{out} and through the unfiring (I_u) and firing (I_f) sections of a PND with 6 sections and integrated resistors (6-PND-R) and for the number of firing sections n ranging from 1 to 6. As n increases, the peak values of the output current (I_{out}, Figure 4.b) and of the current through the unfiring sections (I_u, Figure 4.c) increase. The firing sections experience a large drop in their current (I_f, Figure 4.d), which is roughly independent on n. The observed temporal dynamics will be examined in the following sections.

5.2 Current redistribution and efficiency

Let $\overline{\delta I_{lk}}^{(n)}$ be the peak value of the leakage current drained by each of the still superconducting (unfiring) nanowires when n sections fire simultaneously. The stability requirement translates in the condition that for each unfiring section: $I_B + \overline{\delta I_{lk}}^{(n_{max})} \leq I_C$ (as the leakage current increases with n, $\overline{\delta I_{lk}}^{(n_{max})}$ represents the worst case). This limits the bias current and therefore the single-photon detection efficiency (η), which, for a certain nanowire geometry (i.e. w, t fixed), is a monotonically increasing function of I_B/I_C (Verevkin et al. 2002). For instance, to detect a single photon (at λ=1.3 μm, T=1.8K) in a section with an efficiency equal to 80% of the maximum value set by absorption (~32%, (Gol'tsman et al. 2007)), $\overline{\delta I_{lk}}^{(n_{max})}$ should be made ≤33% of I_B. Therefore the leakage current strongly affects the performance of the device and it is to be minimized, which makes it very important to understand its dependency from the design parameters: $\overline{\delta I_{lk}}^{(n)}(N, L_0, R_0, R_{out})$.

The leakage current can be investigated just in the case of n=1, as the design guidelines drawn from this analysis still apply to higher n (Marsili et al. 2009b). The dependency of $\overline{\delta I_{lk}}^{(1)}$ on N and L_0 at fixed R_0 and R_{out} (both equal to 50 Ω) is shown in Figure 5.a: an orange line highlights bare devices (L_0=L_{kin}, see Table 1) and the colored bars are relative to devices which respect the constraints on the geometry of the structure (L_0>L_{kin}), while the grey bars refer to purely theoretical devices which just show the general trend. For any N, the current redistribution increases with decreasing L_0, as the impedance of each section decreases. Keeping L_0 constant, $\overline{\delta I_{lk}}^{(1)}$ decreases with increasing N, as the current to be redistributed is fixed and the number of channels draining current increases. For this reason also the increase of redistribution with decreasing L_0 becomes weaker for high N.

The dependency of $\overline{\delta I_{lk}}^{(1)}$ on R_0 and R_{out} (for the same N, L_0) is very intuitive (Marsili et al. 2009b). Indeed, the redistribution decreases as R_0 increases because the impedance of each section increases with respect to the output resistance. For the same reason, $\overline{\delta I_{lk}}^{(1)}$ is strongly reduced when R_{out} is decreased.

In conclusion, the result of this simplified analysis is that, to minimize the leakage current and thus maximize the efficiency, N, L_0 and R_0 must be made as high as possible and R_{out} as low as possible. We note however that R_0 cannot be increased indefinitely to avoid that the nanowire latches to the hotspot plateau before I_B reaches I_C (Marsili et al. 2008).
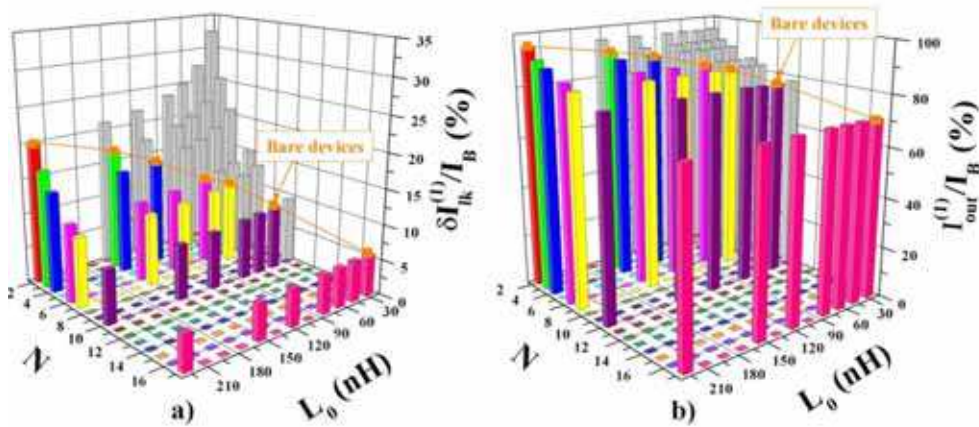
Fig. 5. Peak value of the leakage current $\overline{\delta \mathbf{I}}_{lk}^{(1)}$ drained by each of the still superconducting (unfiring) nanowires (a) and of the output current $\overline{\mathbf{I}}_{out}^{(1)}$ (b) when only one section fires plotted as a function of the number of sections in parallel N and of the value of the inductance of each section L_0. The leakage current and the output current are expressed in % of the bias current I_B because they are proportional to it. From (Marsili et al. 2009b).

5.3 Transient response and speed

Before proceeding to the analysis of the SNR and speed performances of the device, it is necessary to discuss the characteristic recovery times of the currents in the circuit.

The transient response of the simplified equivalent electrical circuit of the N-PND (Figure 4.a) to an excitation produced in the firing branch can be found analytically. Therefore, the transient response of the current through the firing sections I_f, through the unfiring sections I_u and through the output I_{out} after the nanowires become superconducting again (t≥t$_{hs}$) can be written as:

$$\begin{cases} I_f \propto \dfrac{N-n}{N}\exp\left(-t/\tau_s\right) + \dfrac{n}{N}\exp\left(-t/\tau_f\right) \\[2mm] I_u \propto \exp\left(-t/\tau_s\right) - \exp\left(-t/\tau_f\right) \\[2mm] I_{out} \propto \exp\left(-t/\tau_f\right) \end{cases} \tag{3}$$

where $\tau_s = L_0/R_0$ and $\tau_f = L_0/(R_0 + N R_{out})$ are the "slow" and the "fast" time constant of the circuit, respectively. This set of equations describes quantitatively the time evolution of the currents after the healing of the hotspot in the case $\tau_f \gg t_{hs}$, and it provides a qualitative understanding of the recovery dynamics of the circuit for shorter τ_f.

The recovery transients (t≥t$_{hs}$) of I_{out}, δI_{lk} and I_f for a 4-PND-R simulated with the circuit of figure Figure 4.a are shown in figure 6a, b, c, respectively (in blue) for different number of firing sections (n=1 to 4). As n increases from 1 to 4, the recoveries of I_{out} and δI_{lk} change only by a scale factor. On the other hand, the transient of I_f depends on n and becomes faster increasing n, as qualitatively predicted by the first of equations (3). Indeed, I_f consists in the

sum of a slow and a fast contribution, whose balance is controlled by the number of firing sections n. To prove the quantitative agreement with the analytical model in the limit $\tau_f \gg t_{hs}$, the simulated transients of I_{out}, δI_{lk} and I_f have been fitted (figure 6a, b, c, respectively, in red) using the set of equations (3), and four fitting parameters (τ_s, τ_f, a time offset t_0 and a scaling factor K). The values of τ_s and τ_f obtained from the three fittings (of I_{out}, of δI_{lk} and of the whole set of four I_f for $n=1,\ldots, 4$) closely agree with the values calculated from the analytical expressions presented above and the parameters of the circuit (τ_s^*=2.30 ns ,τ_f^*=460 ps).

To quantify the speed of the device, we take $f_0=(t_{reset})^{-1}$ as the maximum repetition frequency, where t_{reset} is the time that I_f needs to recover to 95% of the bias current after a detection event. According to the results presented above, which are in good agreement with experimental data (Figure 2.b), I_{out} decays exponentially with the same time constant for any n ($\tau_{out}=\tau_f$), which, for a bare N-PND, is N^2 times shorter than a normal SSPD of the same surface (Gol'tsman et al. 2007; Tarkhov et al. 2008). This however does not relate with the speed of the device. Indeed, t_{reset} is the time that the current through the firing sections I_f needs to rise back to its steady-state value ($I_f \sim I_B$). In the best case of $n=N$, I_f rises with the fast time constant τ_f, but in all other cases the slow contribution becomes more important as n decreases (see Figure 4.d and figure 6.c), until, for $n=1$, $I_f \sim [1-\exp(-t/\tau_s)]$. The speed performance of the device is then limited by the slow time constant ($t_{reset} \sim 3 \cdot \tau_s$), which means that an N-PND is only N times faster than a normal SSPD of the same surface, being as fast as a normal SSPD whose kinetic inductance is the same as one of the N section of the N-PND.

5.4 Signal to noise ratio

The peak value and the duration of the output current pulse are a function of the design parameters (see below and section 5.3, respectively). As the output pulse becomes faster, amplifiers with larger bandwidth are required and thus electrical noise become more important. To assess the possibility to discriminate the output pulse from the noise, we define the signal to noise ratio (SNR) as the ratio between the maximum of the output current $\bar{I}_{out}$ and the rms value of the noise-current at the preamplifier input I_n, $SNR=\bar{I}_{out}/I_n$.

The peak value of the output current when n sections fire simultaneously (see Figure 4.b, relative to a 6-PND-R) can be written as:

$$I_{out}^{(n)} = n\left(I_B - I_f^{(n)*}\right) - \left(N-n\right)\delta I_{lk}^{(n)*}$$

where the starred values refer to the time $t=t^*$ when the output current peaks.

As $n=1$ represents the worst case, to evaluate the performance of the device in terms of the SNR, the dependency of $\bar{I}_{out}^{(1)}$ from the design parameters is investigated: $\bar{I}_{out}^{(1)}\left(N,L_0,R_0,R_{out}\right)$.

The dependency of $\bar{I}_{out}^{(1)}$ on N and L_0 at fixed R_0 and R_{out} (both equal to 50 Ω) is shown in Figure 5.b. Inspecting the values of $\bar{I}_{out}^{(1)}$ and $\overline{\delta I}_{lk}^{(1)}$ for the same device in Figure 5, it becomes clear that they add up to a value well above to I_B, which is due to the fact that the output current and of the leakage current peak at two different times t^* and t_{lk}, respectively (Figure 4.b, c). Furthermore, as $t_{lk}>t^*$, the output current is not significantly affected by redistribution, because I_{out} is maximum when δI_{lk} is still beginning to rise.
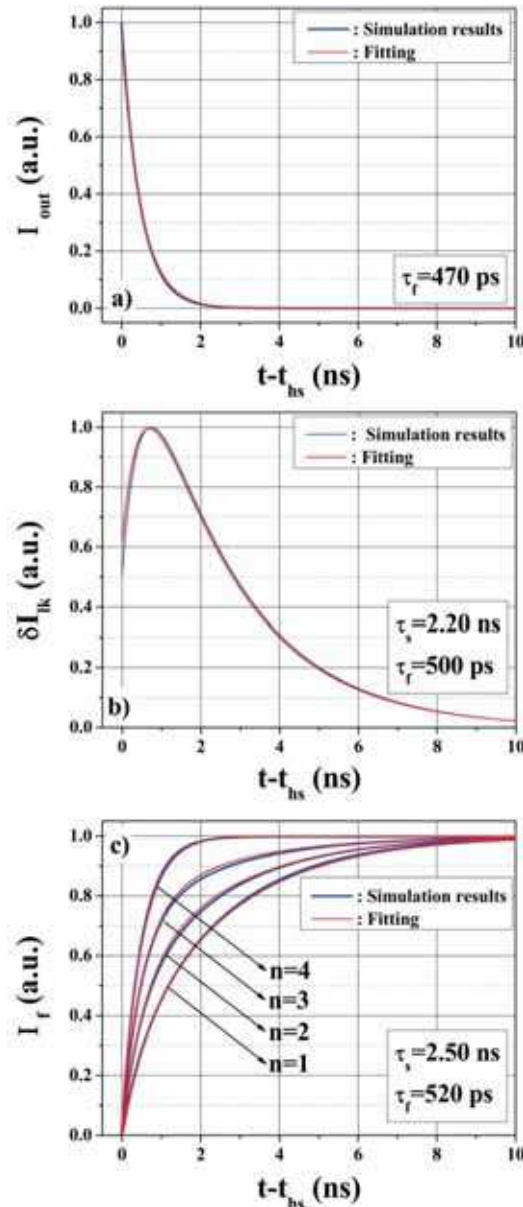
Fig. 6. Recovery transients (t≥t_{hs}) of I_{out} (a), δI_{lk} (b), and I_f (c) for a 4-PND-R as n increases from 1 to 4. The simulated transients are in blue, the fitted curves are in red. The parameters of the circuit used for the simulations are: L_0=L_{kin}=117 nH, R_0=50 Ω, R_{out}=50 Ω, R_{hs}=5.5 kΩ, and t_{hs}=250ps. The three sets of curves are fitted by equations (3) (multiplied by K, and shifted by t_0), where the values of τ_s and τ_f are shown in the insets. From (Marsili et al. 2009b).

The expression for t_{lk} can be derived from (3): $t_{lk}= L_0/(N \cdot R_{out})\ln(1+N \cdot R_{out}/R_0)$, which means that increasing the device speed (decreasing L_0 or R_0, N or R_{out}) makes the redistribution faster and then $\overline{I}_{out}^{(1)}$ lower.

So, for any given N, $\overline{I}_{out}^{(1)}$ decreases (Figure 5.b) with decreasing L_0, both because $\overline{\delta I}_{lk}^{(1)}$ is higher and because t_{lk} is lower. Keeping L_0 constant, $\overline{I}_{out}^{(1)}$ decreases with increasing N because even though $\overline{\delta I}_{lk}^{(1)}$ decreases, the redistribution peaks earlier and the number of channels draining current increases.

The redistribution speed-up explains the dependency of $\overline{I}_{out}^{(1)}$ on R_0 (for the same N, L_0). Indeed, even though $\overline{\delta I}_{lk}^{(1)}$ decreases as R_0 increases (see section 5.2), the output current decreases due to the decrease of t_{lk}: $\delta I_{lk}^{(1)*}$ increases despite the decrease of the peak value of the leakage current. On the other hand, a decrease in R_{out} makes the redistribution much less effective, as t_{lk} decreases slower with decreasing R_{out} than with increasing R_0 (Marsili et al. 2009b).

In conclusion, to maximize the output current, N, R_0 and R_{out} must be minimized, while L_0 must be made as high as possible.

The rms value of noise-current at the preamplifier input I_n can be written as $I_n = \sqrt{S_n \Delta f}$, where S_n is the noise spectral power density of the preamplifier and Δf is the bandwidth of the output current I_{out}, which is estimated as $\Delta f = 1/\tau_{out}$, where $\tau_{out} = \tau_f = L_0/(R_0 + N R_{out})$ is the time constant of the exponential decay of I_{out} (see sec. 5.3). I_n is then a function of the parameters of the device and of the read-out through S_n and τ_f, and like I_{out} it is minimized minimizing N, R_0 and R_{out} and maximizing L_0.
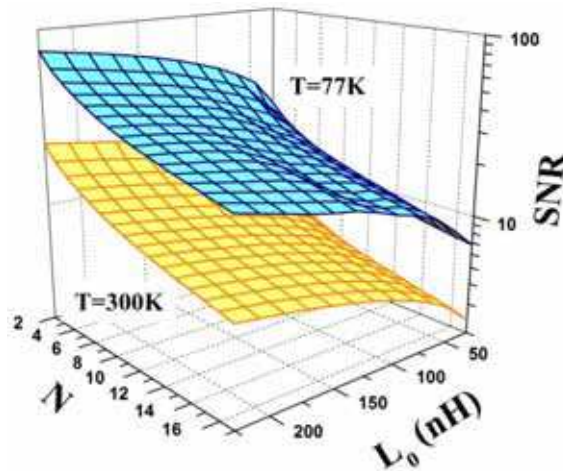

Fig. 7. SNR as a function of N and L_0 relative to commercially available cryogenic (77 K working temperature, in blue) and room-temperature amplifiers (in yellow). For the cryogenic amplifiers the following noise figures were used, relative to different -3 dB bandwidths: F=0.44 dB (Δf=0.1-4 GHz), F=1.3 dB (Δf=0.5-20 GHz), F=1.8 dB (Δf=0.5-40 GHz). For the room-temperature amplifiers: F=1.1 dB (Δf=0.1-4 GHz), F=2.13 dB (Δf=0.1-20 GHz), F=5 dB (Δf=0.1-40 GHz).

The same optimization criteria apply then naturally to the SNR. The dependence of the SNR from N and L_0 is shown in Figure 7 for cryogenic (77 K working temperature, in blue) and room-temperature amplifiers (in yellow). Amplifiers with different -3 dB bandwidths have been considered, depending on the bandwidth of the output current pulse that they were supposed to amplify. Depending on the amplifier bandwidth, noise figures of F=0.44 to 1.8 dB (F=1.1 to 5 dB) have been considered in the calculation of Sn for the room-temperature (cryogenic) amplifier. The input resistance is R_{out}=50Ω.

The main design guidelines which can be deduced from the analysis of sections 5.2 to 5.4 are summarized in Table 2. The type of dependency of $\overline{\delta I}_{lk}$, f_0, $\overline{I}_{out}$ and I_n from the design parameters (L_0, R_0, R_{out}, N) is indicated.

	L_0	R_0	R_{out}	N
δI_{lk}	↘	↘	↗	↘
f_0	↘	↗	--	--
I_{out}	↗	↘	↘	↘
I_n	↘	↗	↗	↗

Table 2. Dependency of the figures of merit from the design parameters: increasing with increasing the parameter (↗), decreasing with increasing the parameter (↘), independent (−−).

6. Application to the measurement of photon number statistics

We wish to determine whether the PND can be used to measure an unknown photon number probability distribution **S** (see section 4.3). Indeed, the light statistics measured with a PND differ from the original one due to non-idealities such as the limited number of sections and limited and non-uniform efficiencies (η_i) of the different sections.

In this section, we present the modeling tools (section 6.1) used to fully characterize the device (section 6.2) (Marsili et al. 2009a) and to develop an algorithm to estimate the photon number statistics of an unknown light (section 6.3) (Marsili et al. 2009b).

6.1 Modeling and simulation

Equation (1) may be rewritten in a matrix form as **Q=P^N·S**, where $P^N = \left[P^N(n|m) \right] = \left[p_{nm}^N \right]$ is the matrix of the conditional probabilities of an N-PND. Assuming that the illumination of the device is uniform, the parallel connection of N nanowires can be considered equivalent to a balanced lossless N-port beam splitter, every channel terminating with a single photon detector (SPD) (Figure 8.a). Each incoming photon is then equally likely to reach one of the N SPDs (with a probability $1/N$). Each SPD can detect a photon with a probability η_i (i=1,..,N) different from all the others, and gives the same response for any number ($n \geq 1$) of photons detected (Figure 8.b). The number of SPDs firing then gives the measured photon number. Two classes of terms in P^N can be calculated directly, the others being derived from these by a recursion relation (Divochiy et al. 2008; Marsili et al. 2009a). These terms are the probabilities $p_{m,m}^N$ that all the $m \leq N$ photons sent are detected and $p_{0,m}^N$ that no photons are detected when m are sent.
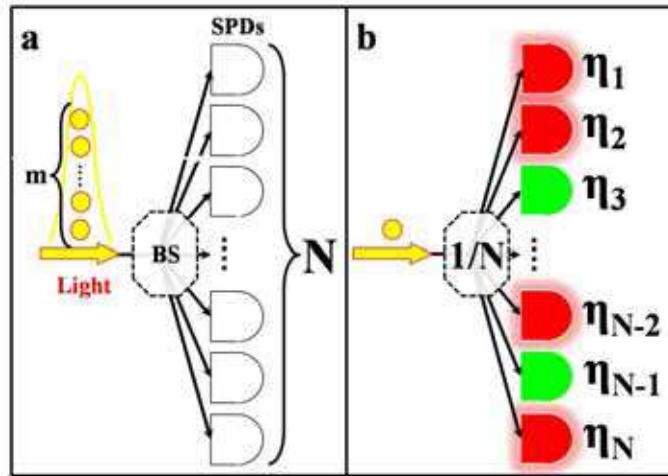
Fig. 8. a. Optical equivalent of an *N*-PND. b. *k*th possible configuration of *n* firing (red) and *N-n* unfiring (green) sections. Each incoming photon is equally likely to reach one of the *N* SPDs (with a probability $1/N$). Each SPD can detect a photon with a probability η_i (i=1,..,N) different from all the others, and it gives the same response for any number ($n \geq 1$) of photons detected. From (Marsili et al. 2009a).

In the case of zero detections, $p_{0,m}^{N}$ is given by:

$$p_{0,m}^{N} = \sum_{i_1=1,\ldots,i_m=1}^{N} \left[\frac{1-\eta_{i_1}}{N} \cdot \ldots \cdot \frac{1-\eta_{i_m}}{N} \right] \tag{4}$$

which assumes that a photon incident in the ith nanowire fails to be detected with an independent probability of (1-η_i). The sum in (4) accounts for all the possible combinations when taking *m* elements in an ensemble of *N* with order and with repetition (permutations with repetitions). This because more than one photon can hit the same stripe (which gives the repetition), and the photons are considered distinguishable (which gives the order).

In the case that all the photons are detected, since *m* photons must reach *m* distinct nanowires:

$$p_{m,m}^{N} = \sum_{\substack{i_1=1,\ldots,i_m=1 \\ i_p \neq i_q \ for \ p \neq q}}^{N} \left[\frac{\eta_{i_1}}{N} \cdot \ldots \cdot \frac{\eta_{i_m}}{N} \right] \quad \text{for } m \leq N \tag{5}$$

The sum in (5) accounts for all the possible combinations when taking *m* elements in an ensemble of *N* with order and without repetition (permutations without repetitions). This because only one photon can hit the same stripe (which gives the non-repetition), and the photons are considered distinguishable (which gives the order).

The recursion relation for p_{nm}^{N} is:

$$p_{nm}^{N} = p_{n,m-1}^{N} \left[\frac{n}{N} + \frac{n!}{N!} \cdot \sum_{\substack{i_1=1,\dots,i_{N-n}=1 \\ i_p \neq i_q \ for \ p \neq q}}^{N} \left(\frac{1-\eta_{i_1}}{N} + \dots + \frac{1-\eta_{i_{N-n}}}{N} \right) \right] +$$

$$+ p_{n-1,m-1}^{N} \left[\frac{(n-1)!}{N!} \cdot \sum_{\substack{i_1=1,\dots,i_{N-(n-1)}=1 \\ i_p \neq i_q \ for \ p \neq q}}^{N} \left(\frac{1-\eta_{i_1}}{N} + \dots + \frac{1-\eta_{i_{N-(n-1)}}}{N} \right) \right]$$

(6)

The first term on the right-hand side of (6) is the probability that n photons are detected when m-1 are sent, times the probability that the mth photon reaches one of the n nanowires already occupied (first term in the square brackets) or that it fails to be detected reaching one of the N-n unoccupied nanowires (second term in the square brackets). To clarify how the latter probability is derived, it is sufficient to consider a particular configuration k (see Figure 8.b) of n firing stripes (which have already detected a photon) and N-n unfiring stripes (still active). The probability that the incoming photon will not be detected when incident on any of the N-n unfiring stripes is then written as:

$$p_k = \frac{1-\eta_{i_1}}{N} + \dots + \frac{1-\eta_{i_{N-n}}}{N}$$

(7)

where $i_1 \dots i_{N-n}$ are the N-n stripes active in the kth configuration of (n)firing-(N-n)unfiring stripes considered. So a mean must be calculated on all the possible (n)firing-(N-n)unfiring configurations for the N stripes. Let C be the number of all these configurations. The mean is then calculated summing C terms of the type (7), and dividing by C: $1/C \cdot \sum_{k=1}^{C} p_k$. C is the number of permutations without repetitions of N-n elements in an ensemble of N, and it is given by the binomial coefficient: $C = N!/\left(N-(N-n)\right)! = N!/n!$. The second term on the right-hand side of (6) is the probability that n-1 photons are detected when m-1 are sent times the probability that the mth photon reaches one of the N-(n-1) unoccupied nanowires and it is detected.

To prove the consistency of the analytical model, the probability distribution of the number of measured photons **Q** calculated from P^N by (1) was cross-checked with the **Q$_{MC}$** resulting from a Monte Carlo simulation (Marsili et al. 2009a). The input parameters of the simulation are the incoming photon number probability distribution **S**, the number of parallel stripes N, and the vector of the single-photon detection efficiencies of the different sections of the device $\boldsymbol{\eta}=[\eta_i]$.

6.2 Matrix of conditional probabilities

It has been shown (Achilles et al. 2004; Lee et al. 2004) that an unknown incoming photon number distribution **S** can be recovered if **Q** and **P^N** are known.

Let an N-PND be probed with a light whose photon number probability distribution is **S**, and its output be sampled H times. The result of the observation can be of N+1 different types (i.e. 0,..., N stripes firing), so an histogram of the H events can be constructed, which can be represented by a (N+1)-dimensional vector **r**=[r_i], where r_i is the number of runs in which the outcome was of the ith type. The expectation value of the statistics obtained from the histogram is E[**Q$_{ex}$**=**r**/H]=**Q**. Considering equations (4) to (6), it is clear that the matrix of

the conditional probabilities of a N-PND depends only on the vector of the N single-photon detection efficiencies of the different sections of the device $\eta=[\eta_i]$. The vector η can be determined from the statistics $\mathbf{Q_{ex}}$ measured when probing the device with a light of known statistics $\mathbf{S}$ as described in the following.

A 5-PND (A_d=8.6x8 µm²) was tested with the coherent emission from a mode-locked Ti:sapphire laser under uniform illumination, whose photon number probability distribution is close to a Poissonian and could be fully characterized by the mean photon number µ with a power measurement. To determine $\mathbf{Q_{ex}}$, histograms of the photoresponse voltage peak V_{pk} were built for values of µ ranging from ~1 to ~100. The signal from the device was sent to the 1 GHz oscilloscope, which was triggered by the synchronization generated by the laser unit. The photoresponse was sampled for a gate time of 5ps, making the effect of dark counts negligible. The discrete probability distribution $\mathbf{Q_{ex}}$ was reconstructed from the continuous probability density q(V_{pk}) fitting the histograms to the sum of 6 Gaussian distributions (corresponding to the five possible pulse levels plus the zero level) and calculating their area (Figure 9).
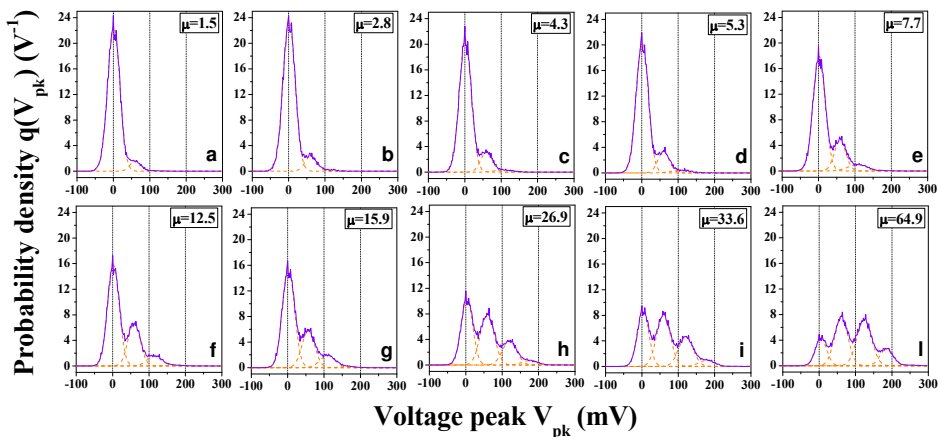

Fig. 9. Histograms of the photoresponse voltage peak. The 5-PND was tested in a dipstick dipped in a liquid He bath at 4.2 K. The light pulses at 700nm form the mode-lock Ti:sapphire laser were 40ps wide (after the propagation in the optical fiber) and the repetition rate was 80MHz. The average input photon number per pulse µ was set with a free space variable optical attenuator. Increasing µ, form 1.5 (a) to 64.9 (l), the shape of the histograms changes as the probability to observe higher response amplitudes increases. The solid lines are the experimental histograms. The dashed lines represent the fitted Gaussian distribution of each possible pulse level. From (Marsili et al. 2009a).

The probability distribution of the number of measured photons $\mathbf{Q}$ (expressed by(1)) was then fitted to the experimentally measured distribution $\mathbf{Q_{ex}}$ using η as a free parameter (Figure 10). The resulting η and matrix of the conditional probabilities are shown in Figure 11. The fitted efficiencies are rather uniform (2.9±0.5%), indicating a high-quality fabrication process. The value of η obtained from the fitting was then used as an input parameter of Monte Carlo simulations (see above) used to calculate $\mathbf{Q_{MC}}$ for each value of µ. The three sets of values for the photocount statistics of six levels are in good agreement over almost two orders of magnitude of µ, confirming the validity of the analytical model.
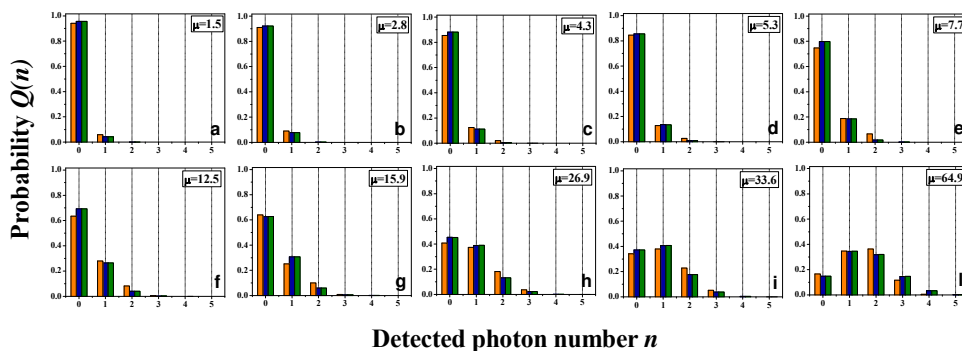
Detected photon number *n*

Fig. 10. Experimental (Q_{ex}), fitted (Q) and simulated (Q_{MC}) probability distributions of the number of measured photons. The experimental probability distribution Q_{ex} (orange bins) was estimated from the continuous probability density $q(V_{pk})$ of Figure 9. The 5-PND was probed with several incident mean photon numbers µ: 1.5, 2.8, 4.3, 5.3, 7.7, 12.5, 15.9, 26.9, 33.6, 64.9. The experimental values for Q_{ex} were then fitted (blue bins) using a genetic algorithm to recover the vector of detection efficiencies η. The value of η obtained was used to calculate Q_{MC} for each value of µ by Monte Carlo simulations (green bins). From (Marsili et al. 2009a).
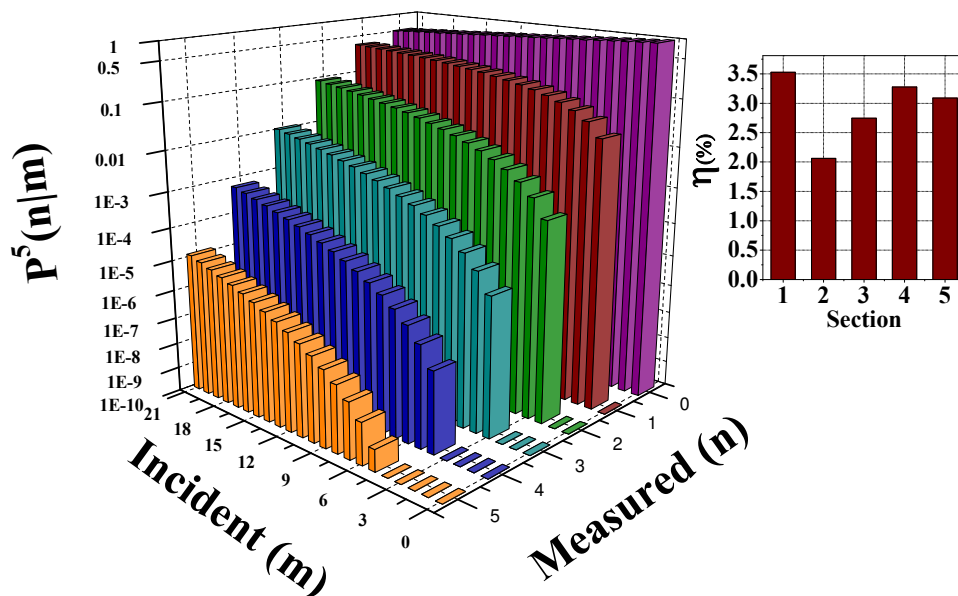

Fig. 11. Conditional probability matrix for a 8.6x8 µm² 5-PND (with no integrated series resistors), calculated from the vector η of the 5 single-photon detection efficiencies (relative to T=4.2 K, λ=700nm) of the different sections of the device (inset). From (Marsili et al. 2009b).

6.3 Maximum-Likelihood (ML) estimation

i. ML method

The $\mathbf{P^N}$ matrix provides a full description of the detector. Once $\mathbf{P^N}$ is known, several approaches can be used to reconstruct $\mathbf{S}$ from the histogram $\mathbf{r}$. In the case no assumptions on the form of $\mathbf{S}$ are made, the maximum likelihood (ML) method is the most suitable, as it is the most efficient in solving this class of problems (Eadie et al.).

Let $\mathbf{R}= R_0,\ldots, R_N$ be the random vector of the populations of the $(N+1)$ different bins of the histogram after H observations. The joint probability density function L($\mathbf{r}|\mathbf{Q}$) for the occurrence of the particular configuration $\mathbf{r}=r_0,\ldots, r_N$ of $\mathbf{R}$ is called the likelihood function of $\mathbf{r}$ and it is given by (Eadie et al.):

$$L\left(\mathbf{r}|\mathbf{Q}\right) = H!\prod_{i=0}^{N}\frac{q_i^{r_i}}{r_i!} \tag{8}$$

where $\mathbf{Q}=[q_i]$ is the probability distribution of the number of measured photons, i.e. the vector of the probabilities to have an outcome in the bin i (i=0,$\ldots$, N) in a single trial.

Considering $\mathbf{Q}$ as a function of $\mathbf{S}$ through (1), we can rewrite the likelihood function of the vector $\mathbf{r}$, depending on the parameter $\mathbf{S}$:

$$L\left(\mathbf{r}|\mathbf{S}\right) = H!\prod_{i=0}^{N}\frac{\left(\sum_m p_{i,m}^N s_m\right)^{r_i}}{r_i!} \tag{9}$$

which is then the probability of the occurrence of the particular histogram $\mathbf{r}$ when the incoming light has a certain statistics $\mathbf{S}$.

As $\mathbf{r}$ is measured and then it is known, L($\mathbf{r}|\mathbf{S}$) can be regarded as a function of $\mathbf{S}$ only, i.e. L($\mathbf{r}|\mathbf{S}$) is the probability that a certain vector $\mathbf{S}$ is the incoming probability distribution when the histogram $\mathbf{r}$ is measured. The best estimate of the incoming statistics which produced the histogram $\mathbf{r}$ according to the ML method is the vector $\mathbf{S_e}$ which maximizes L($\mathbf{r}|\mathbf{S}$), where $\mathbf{r}$ is treated as fixed. So, the estimation problem can in the end be reduced to a maximization problem.

ii. Description of the algorithm

For numerical calculations, it is necessary to limit the maximum number of incoming photons to m_{max} (in the following calculations, $m_{max}=21$). As $\mathbf{S}$ is a vector of probabilities, the maximization must be carried out under the constraints that the s_n are positive and that they add up to one. The positivity constraint can be satisfied changing variables: $s_n=\sigma_n^2$. Instead of L, we maximize the logarithm of L:

$$l\left(\Sigma\right) = \ln\left(L\left(\Sigma\right)\right) = \ln\left(C\right) + \sum_{i=0}^{N} r_i \ln\left(\sum_{m=0}^{m_{max}} p_{i,m}^N \sigma_m^2\right) \tag{10}$$

where $\Sigma=[\sigma_n]$ and C is a constant. The condition that the s_n add up to one can be taken into account using the Lagrange multipliers method: $F\left(\Sigma,\alpha\right)=l\left(\Sigma\right)-\alpha\left(\sum_{m=0}^{m_{max}}\sigma_m^2-1\right)$.

After developing (Banaszek 1998) the set of $m_{max}+2$ gradient equations $\nabla F\left(\Sigma,\alpha\right)=0$, we obtain that $\alpha=H$ and that the set of $m_{max}+1$ nonlinear equations to be solved respect to Σ is:

$$\sigma_l \left[\sum_{i=0}^{N} \frac{r_i p_{i,l}^{N}}{\sum_{m=0}^{m_{max}} p_{i,m}^{N} \sigma_m^2} - H \right] = 0 \qquad (11)$$

for l=0,…, m_{max}. The set of equations (11) can be solved by standard numerical methods.

iii. ML reconstruction

To test the effectiveness of the reconstruction algorithm, a 8.6x8 µm^2 5-PND was tested with the coherent emission from a mode-locked Ti:sapphire laser. $\mathbf{Q_{ex}}$ was determined as described in section 6.2.

The device was already characterized in terms of its conditional probability matrix $\mathbf{P^5}$ (Figure 11), so it was possible to carry out the ML estimation of the different incoming distributions with which the device was probed. Because of the bound on the number of incoming photons which is possible to represent in our algorithm (m_{max}=21) and as, for a coherent state, losses simply reduce the mean of the distribution, the ML estimation was performed considering $\mu^*=\mu/10$ and $\boldsymbol{\eta}^*=10\boldsymbol{\eta}$ (the efficiency of each section being lower than 10%).

Figure 12 shows the experimental probability distribution of the number of measured photons $\mathbf{Q_{ex}}$ obtained from the histograms measured when the incoming mean photon number is µ=1.5, 2.8, 4.3 photons/pulse (Figure 12.a, b, c respectively, in red), from which the incoming photon number distribution is reconstructed. The ML estimate of the incoming probability distribution $\mathbf{S_e}$ is plotted in Figure 12.d, e, f, (green), where it is compared to the real incoming probability distribution $\mathbf{S}$ (blue). The estimation is successful only for low photon fluxes (µ=1.5, 2.8 Figure 12.d, e) and it fails already for µ=4.3 (Figure 12.f). In Figure 12.a, b, c, $\mathbf{Q_{ex}}$ (red) is compared to the ones obtained from $\mathbf{S}$ and $\mathbf{S_e}$ through relation (1) ($\mathbf{Q}$, $\mathbf{Q_e}$ in blue and green, respectively).

The main reasons why the reconstruction fails are not the low efficiencies of the sections of the PND or the spread in their values, but rather the limited counting capability (*N*=5) and a poor calibration of the detector, i.e. an imperfect knowledge of its real matrix of conditional probabilities. This assessment is supported by the following argument. If we generate $\mathbf{Q_{ex}}$ with a Monte Carlo simulation (see section 6.1) using the same $\boldsymbol{\eta}$ vector of Figure 11 and a Poissonian incoming photon number distributions and then we run the ML reconstruction algorithm (using the same $\mathbf{P^5}$, which this time describes perfectly the detector), $\mathbf{S}$ can be estimated up to much higher mean photon numbers (µ≥16, see Figure 13). Additional simulations will be needed to evaluate the performance of PNDs for the measurement of other, nonclassical photon number distributions. However, to alleviate this problem, a self-referencing measurement technique might be used (Achilles et al. 2006).

7. Discussion on the counting capability

Several factors may limit the counting capability (M_{max}) of a PNR detector.

One is the detection efficiency. From (5), assuming the detector saturation is negligible (*n*<<*N*) and that all the branches are equal ($\eta_i=\eta$), the probability Q(*n*) of detecting *n* photons is proportional to η^n. In the PND tested $\tilde{\eta}\sim2\%$ at 1.3 µm (section 4.3), which we attribute to unoptimised film thickness and device design. This obviously prevents the application of the present device to *n*-photon states measurement for *n*>>1. Nevertheless, the η of SSPDs,
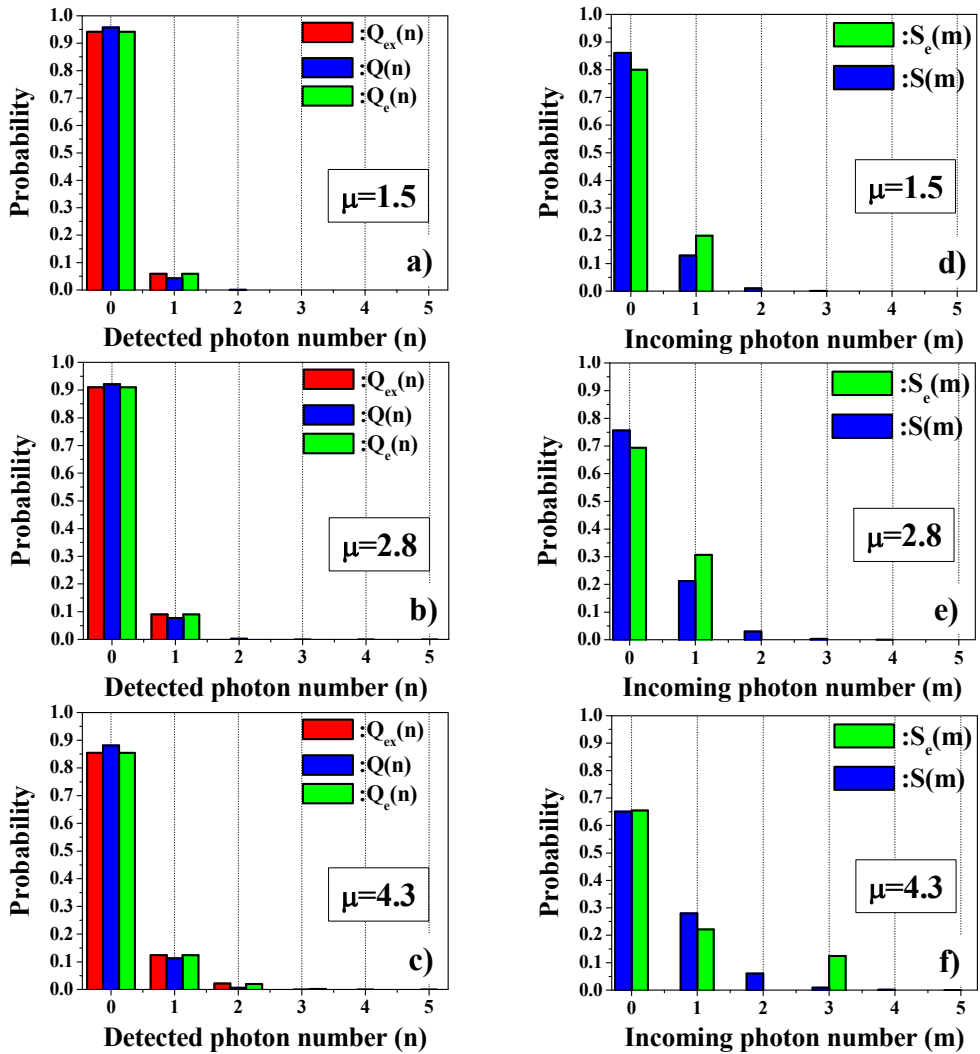
Fig. 12. a, b, c. Probability distribution of the number of measured photons obtained from experimental data Q_{ex} (red) from S (Q, in blue) and S_e (Q_e, in green) through relation (1), for μ=1.5, 2.8, 4.3 photons/pulse, respectively. d, e, f. Real incoming probability distribution S (blue) and its ML estimate S_e (green) for μ=1.5, 2.8, 4.3 photons/pulse, respectively. From (Marsili et al. 2009b).
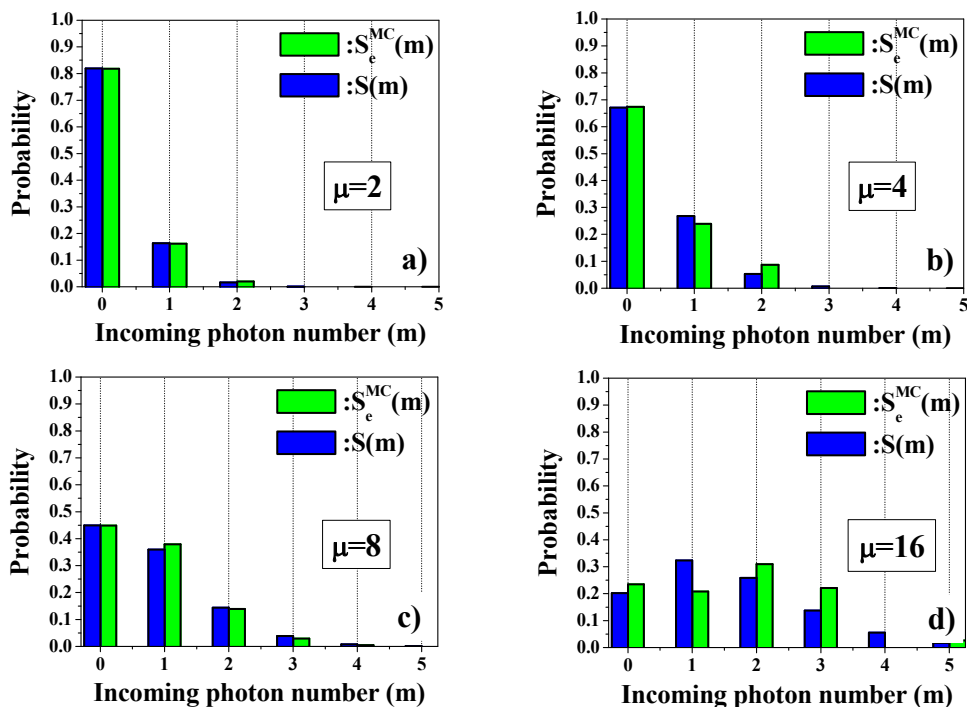
Fig. 13. Real incoming probability distribution S (blue) and its ML estimate S_e^{MC} (green), reconstructed from a Q_{ex} generated with a Monte Carlo simulation (see section 6.1) using the same η vector of Figure 11 for μ=2 (a), 4 (b), 8 (c), 16 (d) photons/pulse.

which are based on the same detection mechanism, can be increased up to ~60% (Rosfjord et al. 2006), and could potentially exceed 90% using optimized optical cavities. We also stress that uniform illumination of the wires is needed to achieve the optimum performance.

The second limitation is the intrinsic noise of the detector. As the currents from the sections of the PND are summed up to build the output, pulse height discrimination is used to achieve photon number resolution. This makes the noise performance of the device critical for its counting capability, as independent noisy signals are summed. Indeed, photon-number discrimination can be performed as long as the noise on the signal amplitude remains lower than the height of the one-photon pulse. The noise properties of any avalanche-based photon counting device are limited by its inner multiplication noise. In other avalanche PNR detectors (Waks et al. 2003; Waks et al. 2004; Zambra et al. 2004; Yamamoto et al. 2006; Fujiwara & Sasaki 2007; Gansen et al. 2007; Kardynal et al. 2007) the amplitude of the output signal is directly proportional to the number of carriers generated by single photon absorption events through a multiplication process which is intrinsically noisy. The noise on the multiplication gain is then completely transferred to the signal, which is then affected by a fluctuation of the same order. In contrast, with PNDs, the noisy avalanche carrier-multiplication process (Semenov et al. 2001) causes a fluctuation only in the resistance R_{hs} of the branch driven normal after the absorption of a photon and not in the

output current. Indeed, the amplitude of the photocurrent peak is determined by the partition between the fluctuating resistance R_{hs} of few kΩ and a resistance R_{out} almost 2 orders of magnitude lower, which is of fixed value. Comparing the broadening of the histogram peaks relative to different numbers of detected photons n (Figure 9), no multiplication noise buildup is observable, as the variance of the peak does not increase with n. The broadening of the peaks is then exclusively due to electrical noise originating from amplifiers and is not a fundamental property of the detector. To a good approximation the excess noise factor F (McIntyre 1966) of the PND is then close to unity and is not limiting M_{max}, which is not the case for most of the other approaches to PNR detection (Waks et al. 2003; Waks et al. 2004; Zambra et al. 2004; Rosenberg et al. 2005; Yamamoto et al. 2006; Fujiwara and Sasaki 2007; Gansen et al. 2007; Kardynal et al. 2007).

In PNDs, a third limitation to M_{max} arises from the leakage current δI_{lk}, which limits the bias current and therefore η. However, as discussed in section 5.2, this issue can be overcome with a careful design of the device.

8. Conclusions

A new PNR detector, the Parallel Nanowire Detector, has been demonstrated (Divochiy et al. 2008; Marsili et al. 2009a), which significantly outperforms existing approaches in terms of sensitivity, speed and multiplication noise in the telecommunication wavelength range. In particular, it provides a repetition rate (80 MHz) three orders of magnitude larger than any existing detector at telecom wavelength (Rosenberg et al. 2005; Fujiwara & Sasaki 2007; Jiang et al. 2007), and a sensitivity (NEP=4.2x10^{-18} W/Hz[1/2]) one-two orders of magnitude better, with the exception of transition-edge sensors (Rosenberg et al. 2005) (which require a much lower operating temperature).

An electrical equivalent model of the device was developed to study its operation and to perform its design (Marsili et al. 2009b). In particular, we found that the leakage current significantly affects only the PND detection efficiency, while it has a marginal effect on its signal to noise ratio. To gain a better insight on the device dynamics, the (N+1)-mesh equivalent circuit of the N-PND was simplified and reduced to a three mesh circuit, so that the analytical expression of its transient response could be easily found. With this approach, we could predict a physical limit to the recovery time of the PND, which is slower than that previously estimated. Furthermore, the figures of merit of the device performance in terms of efficiency, speed and sensitivity ($\overline{\delta I}_{lk}$, f_0, SNR) were defined and their dependency on the design parameters (L_0, R_0, R_{out}, N) was analyzed.

To prove the suitability of the PND to reconstruct an unknown light statistics by ensemble measurements, we developed modeling tools to fully characterize the device and a maximum likelihood estimation algorithm (Marsili et al. 2009a; Marsili et al. 2009b). Testing a 5-PND with a Poissonian light we found that the reconstruction of the incoming photon number probability distribution to be successful only for low photon fluxes, most likely due to the limited counting capability (N=5) and the poor calibration (i.e. the imperfect knowledge of the real matrix of conditional probabilities) of the detector used, and not to its low detection efficiency ($\tilde{\eta} \sim 3\%$). Additional simulations will be needed to evaluate the performance of our detector for the measurement of other, nonclassical photon number distributions. Finally, despite the high sensitivity and speed of PNDs, their present performance in terms of detection efficiency (η=2% at λ=1.3μm) does not allow their application to single shot measurements, as required for linear-optics quantum computing (Knill et al. 2001), quantum repeaters (Sangouard et al. 2007) and conditional-state

preparation (Sliwa & Banaszek 2003). Nevertheless, the η of SPDs based on the same detection mechanism can be increased to ~60% (Rosfjord et al. 2006), and could potentially exceed 90% using optimized optical cavities.

9. Acknowledgments

10. References

Achilles, D., et al. (2004). "Photon-number-resolving detection using time-multiplexing." *J. Mod. Opt.* 51(9-10): 1499-1515.

Achilles, D., et al. (2003). "Fiber-assisted detection with photon number resolution." *Opt. Lett.* 28(23): 2387-2389.

Achilles, D., et al. (2006). "Direct, Loss-Tolerant Characterization of Nonclassical Photon Statistics." *Phys. Rev. Lett.* 97(4): 043602.

Banaszek, K. (1998). "Maximum-likelihood estimation of photon-number distribution from homodyne statistics." *Phys. Rev. A* 57(6): 5013-5015.

Brassard, G., et al. (2000). "Limitations on practical quantum cryptography." *Physical Review Letters* 85(6): 1330-1333.

Dauler, E. A., et al. (2007). "Multi-element superconducting nanowire single-photon detector." *IEEE Trans. Appl. Supercond.* 17(2): 279-284.

Divochiy, A., et al. (2008). "Superconducting nanowire photon-number-resolving detector at telecommunication wavelengths." *Nature Photon.* 2: 302 - 306.

Eadie, W. T., et al. "Satistical Methods in Experimetal Physics." *in Statistical Methods in Experimental Physics, North-Holland, Amsterdam, 1971, Chap 8, and references therein.*

Fitch, M. J., et al. (2003). "Photon-number resolution using time-multiplexed single-photon detectors." *Phys. Rev. A* 68(4 B): 043814

Fujiwara, M. and M. Sasaki (2007). "Direct measurement of photon number statistics at telecom wavelengths using a charge integration photon detector." *Appl. Opt.* 46(16): 3069-3074.

Gansen, E. J., et al. (2007). "Photon-number-discriminating detection using a quantum-dot, optically gated, field-effect transistor." *Nature Photon.* 1: 585-588.

Gol'tsman, G., et al. (2007). "Middle-infrared to visible-light ultrafast superconducting single-photon detectors." *IEEE Trans. Appl. Supercond.* 17(2): 246-251.

Gol'tsman, G. N., et al. (2003). "Fabrication of nanostructured superconducting single-photon detectors." *IEEE Trans. Appl. Supercond.* 13(2 I): 192-195.

Jiang, L. A., et al. (2007). "Photon-number-resolving detector with 10 bits of resolution." *Phys. Rev. A* 75(6): 62325.

Kadin, A. M. *in Introduction to superconducting circuits, Wiley, New York, 1999, Chap 2.*

Kardynal, B. E., et al. (2007). "Photon number resolving detector based on a quantum dot field effect transistor." *Appl. Phys. Lett.* 90(18): 181114.

Kerman, A. J., et al. (2007). "Constriction-limited detection efficiency of superconducting nanowire single-photon detectors." *Appl. Phys. Lett.* 90(10): 101110.

Knill, E., et al. (2001). "A scheme for efficient quantum computation with linear optics." *Nature* 409(6816): 46-52.

Lee, H., et al. (2004). "Towards photostatistics from photon-number discriminating detectors." *J. Mod. Opt.* 51(9-10): 1517-1528.

Lita, A. E., et al. (2008). "Counting near-infrared single-photons with 95% efficiency." *Opt. Express* 16(5): 3032-3040.

Marsili, F., et al. (2009a). "Superconducting parallel nanowire detector with photon number resolving functionality." *J. Mod. Opt.* 56(2-3): 334-344.

Marsili, F., et al. (2008). "High efficiency NbN nanowire superconducting single photon detectors fabricated on MgO substrates from a low temperature process." *Opt. Express* 16(5): 3191-3196.

Marsili, F., et al. (2009b). "Physics and application of photon number resolving detectors based on superconducting parallel nanowires." *New J. Phys.* 11(4): 045022-045043.

Mattioli, F., et al. (2007). "Electrical characterization of superconducting single-photon detectors." *J. Appl. Phys.* 101(5): 054302.

McIntyre, R. J. (1966). "Multiplication noise in uniform avalanche diodes." *IEEE Trans. Electron Devices* 13(1): 164 - 168.

Miller, A. J., et al. (2003). "Demonstration of a low-noise near-infrared photon counter with multiphoton discrimination." *Appl. Phys. Lett.* 83(4): 791-793.

Rosenberg, D., et al. (2005). "Noise-free high-efficiency photon-number-resolving detectors." *Phys. Rev. A* 71(6): 1-4.

Rosfjord, K. M., et al. (2006). "Nanowire Single-photon detector with an integrated optical cavity and anti-reflection coating." *Opt. Express* 14(2): 527-534.

Sangouard, N., et al. (2007). "Long-distance entanglement distribution with single-photon sources." *Phys. Rev. A* 76(5): 050301-4.

Semenov, A. D., et al. (2001). "Quantum detection by current carrying superconducting film." *Physica C* 351(4): 349-356.

Sliwa, C. and K. Banaszek (2003). "Conditional preparation of maximal polarization entanglement." *Physical Review A* 67(3): 030101.

Tarkhov, M., et al. (2008). "Ultrafast reset time of superconducting single photon detectors." *Appl. Phys. Lett.* 92(24): 241112.

Verevkin, A., et al. (2002). "Detection efficiency of large-active-area NbN single-photon superconducting detectors in the ultraviolet to near-infrared range." *Appl. Phys. Lett.* 80(25): 4687.

Waks, E., et al. (2004). "Direct Observation of Nonclassical Photon Statistics in Parametric Down-Conversion." *Phys. Rev. Lett.* 92(11): 113602-1.

Waks, E., et al. (2003). "High-Efficiency Photon-Number Detection for Quantum Information Processing." *IEEE J. Sel. Top. Quant.* 9(6): 1502-1511.

Yamamoto, K., et al. (2006). "Development of Multi-Pixel Photon Counter (MPPC)." *IEEE Nuclear Science Symposium Conference Record, 2006* 2: 1094 - 1097.

Yang, J. K. W., et al. (2007). "Modeling the Electrical and Thermal Response of Superconducting Nanowire Single-Photon Detectors." *IEEE Trans. Appl. Supercond.* 17(2): 581-585.

Yuan, Z., et al. (2002). "Electrically driven single-photon source." *Science* 295(5552): 102-105.

Zambra, G., et al. (2004). "Counting photoelectrons in the response of a photomultiplier tube to single picosecond light pulses." *Rev. Sci. Instr.* 75(8): 2762-2765.

Recent Optical and Photonic Technologies

Edited by Ki Young Kim

Research and development in modern optical and photonic technologies have witnessed quite fast growing advancements in various fundamental and application areas due to availability of novel fabrication and measurement techniques, advanced numerical simulation tools and methods, as well as due to the increasing practical demands. The recent advancements have also been accompanied by the appearance of various interdisciplinary topics. The book attempts to put together state-of-the-art research and development in optical and photonic technologies. It consists of 21 chapters that focus on interesting four topics of photonic crystals (first 5 chapters), THz techniques and applications (next 7 chapters), nanoscale optical techniques and applications (next 5 chapters), and optical trapping and manipulation (last 4 chapters), in which a fundamental theory, numerical simulation techniques, measurement techniques and methods, and various application examples are considered. This book deals with recent and advanced research results and comprehensive reviews on optical and photonic technologies covering the aforementioned topics. I believe that the advanced techniques and research described here may also be applicable to other contemporary research areas in optical and photonic technologies. Thus, I hope the readers will be inspired to start or to improve further their own research and technologies and to expand potential applications. I would like to express my sincere gratitude to all the authors for their outstanding contributions to this book.

How to reference

In order to correctly reference this scholarly work, feel free to copy and paste the following:

Francesco Marsili, David Bitauld, Andrea Fiore, Alessandro Gaggero, Francesco Mattioli, Roberto Leoni, Aleksander Divochiy and Gregory Gol'tsman (2010). Photon-Number-Resolution at Telecom Wavelength with Superconducting Nanowires, Recent Optical and Photonic Technologies, Ki Young Kim (Ed.), ISBN: 978-953-7619-71-8, InTech, Available from: http://www.intechopen.com/books/recent-optical-and-photonic-technologies/photon-number-resolution-at-telecom-wavelength-with-superconducting-nanowires

INTECH
open science | open minds

Fax: +385 (51) 686 166
www.intechopen.com

Fax: +86-21-62489821